Design of a scalable and deformable transparent metasurface with multi-polarization absorptive characteristics based on Miura folding for RCS reduction

Optical Materials EXPRESS

Design of a scalable and deformable transparent metasurface with multi-polarization absorptive characteristics based on Miura folding for RCS reduction

XINHUA MAO, JUNHONG WANG,* ZHAN ZHANG, ZHAOHUA LI, AND YUJIAN LI

Key Laboratory of All Optical Network and Advanced Telecommunication Network, Ministry of Education, Institute of Lightwave Technology, Beijing Jiaotong University, Beijing 100044, China
*wangjunh@bjtu.edu.cn

Abstract: A broadband, scalable, and deformable transparent absorbing metasurface (SDTAM) based on a Miura folding structure is proposed in this paper. The metasurface comprises three indium tin oxide (ITO) resistive film layers and two intermediate rhombic polymethyl methacrylate (PMMA) dielectric layers. The resonant structure integrated into the top layer broadens the working bandwidth. Utilizing an absorption-scattering coordinated regulation mechanism, the electromagnetic scattering behaviors of SDTAM in planar, folded, and conformal states are systematically analyzed. Full-wave simulations and experiments validate the wideband radar cross-section (RCS) reduction performance of the SDTAM. Measurements demonstrate that SDTAM exhibits both optical transparency and excellent mechanical deformability, enabling large-scale expansion and contraction. In the planar state ($\alpha = 90°$), the simulated bandwidth for monostatic RCS reduction of more than 10 dB is achieved from 13.8 to 40 GHz (relative bandwidth of 97.4%) under normal incidence of linearly polarized (LP) and circularly polarized (CP) waves. In the fully folded state ($\alpha = 60°$), the simulated >10 dB monostatic RCS-reduction bandwidth is further extended to 4.1–40 GHz (relative bandwidth of 163%) under normal incidence of LP and CP waves. In addition, stable RCS reduction persists at incident angles up to 70° under normal incidence of LP and CP waves. This design provides an innovative solution for conformal stealth skinning of high-curvature deformable objects.

1. Introduction

In recent years, with the rapid development of radar detection technology, target stealth has been promoted as a research hotspot in electromagnetics [1–4]. As a key parameter for evaluating stealth effectiveness, the radar cross section (RCS) directly determines radar detection range and target recognition probability. Actively controlling RCS through functional skin wrapping over target contours represents a key technical approach for enhancing stealth performance. This method reduces detection probability by precisely regulating electromagnetic wave scattering characteristics on surfaces.

Conventional RCS reduction schemes primarily rely on shape optimization and absorbing materials. While shape optimization enables monostatic RCS suppression by redirecting electromagnetic waves toward non-threatening directions, it suffers from significant frequency dependence and angular limitations [5]. Traditional absorbing materials, including magnetic, dielectric and resistive types, typically exhibit narrow bandwidth, high density and low mechanical strength. In addition, during long-term use, they are prone to cracking and delamination. In high-temperature and humid environments, due to the deterioration of permeability caused by oxidation, their performance drops significantly [6–8].

#605709 https://doi.org/10.1364/OME.605709
Journal © 2026 Received 14 May 2026; revised 24 Jun 2026; accepted 15 Jul 2026; published 24 Jul 2026

Metasurfaces, as two-dimensional artificial electromagnetic structures, manipulate the amplitude, phase, and polarization of electromagnetic waves through subwavelength unit cells, offering a promising approach for broadband, lightweight stealth skins. For instance, Ref. [9] demonstrated full-polarization RCS reduction from 1 to 18 GHz using indium tin oxide (ITO) films and ultra-lightweight foams. Reference [10] designed a planar ultra-wideband absorber using optimization algorithms. Reference [11] achieved more than 20 dB of backward scattering reduction in the band of 8.5 GHz to 20.3 GHz through a cooperative mechanism of absorption and diffuse reflection. These advances collectively demonstrate the broadband stealth capabilities of planar metasurfaces.

In addition to the aforementioned broadband reduction schemes, recent studies have further extended the functionality of planar metasurfaces from static broadband absorption to dynamic multifunctional regulation. For instance, Ref. [12] achieved synergistic control of ultra-low sidelobe beam scanning and in-band radar cross section (RCS) suppression using a space-time-coding radiation-scattering metasurface. Reference [13] demonstrated a continuously tunable metasurface with switchable transmission and absorption modes. Reference [14] realized dynamic meta-holography from linear to nonlinear regimes based on a transmissive independently addressable metasurface. These advances have significantly enhanced the potential of metasurfaces for adaptive manipulation in complex electromagnetic environments. However, the aforementioned dynamic control approaches are limited to planar or quasi-planar configurations. When employed in stealth skins that are required to endure substantial stretching, compression, or conformal attachment to complex curved surfaces, the mechanical incompatibility between the metasurface and the deformable substrate inevitably induces unit-cell distortion and significant degrades electromagnetic performance, which restricts their applicability in adaptive stealth systems. Flexible metasurfaces [15–9] offer a promising alternative. For example, Ref. [15] developed a deformable transparent absorbing metasurface (DTAM) capable of conformal bending with a curvature radius as small as 250 mm. Reference [16] demonstrated a flexible structure achieving both 70.18% average visible transmittance and broadband absorption in the X/Ku bands (8.9 to 16.4 GHz). Although existing flexible metasurfaces can achieve curved surface bonding, they are usually limited to low-curvature surfaces and simple uniaxial stretching, lacking the ability to perform large-scale tensile and compressive deformations. In addition, achieving broadband transparency in deformation technology is also a challenge.

Currently, some existing studies on Miura-ori metasurfaces realized the capabilities of polarization conversion, reflection/scattering modulation, or narrowband RCS/scattering analysis [21–23]. However, none of these efforts can simultaneously achieve broadband multi-polarization RCS reduction, optical transparency, large-scale deployable deformation (tensile and compressive), and systematic verification under planar, folded, and conformal states within a single structure. In contrast, the proposed SDTAM in this work targets broadband RCS reduction throughout the entire folding process, employs a transparent material system (ITO/PET/PMMA), and realizes broadband multi-polarization (horizontal and vertical polarizations) compatibility. Furthermore, through energy proportion decomposition, this work quantitatively reveals the synergistic effect between absorption and structural scattering. The above integration of multiple functionalities and the analysis of the synergistic dissipation mechanism constitute the primary innovation that distinguishes this work from previous Miura-ori metasurface studies. The paper is organized as follows: Section II presents the metasurface design and the underlying absorption mechanism. Section III analyzes the RCS reduction performance in both folded and conformal states, including responses under different polarization angles and oblique incidence. Section IV describes the fabrication and experimental characterization of the prototype sample. Finally, Section V concludes the paper with a summary of key findings and perspectives.

Optical Materials EXPRESS

2. Structure and analysis of metasurface

The unit cell structure of the proposed absorbing metasurface is illustrated in Fig. 1, where Fig. 1(a) shows the three-dimensional configuration, Fig. 1(b) presents the planar topological layout, and Fig. 1(c) gives the detail five-layer stacked architecture. The bottom layer (defined as the first layer) consists of a continuous ITO resistive film (23 nm in thick, 6 Ω/sq) deposited on a 0.188 mm polyethylene terephthalate (PET) substrate ($\varepsilon_r = 3$, tanδ = 0.06). The second layer is a 2 mm thick polymethyl methacrylate (PMMA) dielectric layer ($\varepsilon_r = 2.4$, tanδ = 0.01). The third layer comprises a 200 Ω/sq ITO resistive film on an identical PET substrate. The fourth layer is a 1 mm thick PMMA layer with the same electromagnetic parameters as the second layer. The top layer integrates a patterned ITO film (200 Ω/sq) fabricated through etching. The parallelogram unit cells in bottom-layer incorporate laser-etched crease lines, and their non-rectangular geometry effectively mitigates stress concentration. The upper four layers adopt geometrically similar but downscaled patterns, enabling large deformation through dimensional scaling and providing sufficient space for folding and stretching.

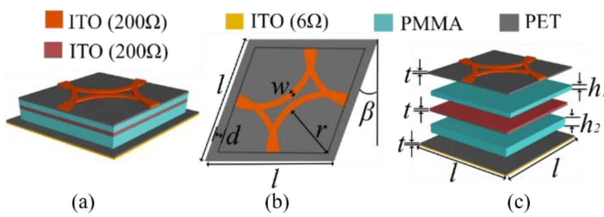

Fig. 1. Structure and parameters of SDTAM metasurface units: (a) 3D view, (b) top view, and (c) layered structure diagram.

Miura-ori, a spatial deployment structure derived from the art of origami, is characterized by its negative Poisson's ratio and large deformation capability. Due to these unique properties, Miura-ori has been introduced into metasurface design to achieve reconfigurability [24–30]. Figure 2 illustrates three configuration states of the absorbing metasurface: the flat state is with a crease angle of 90°, and two folded states are with crease angles of 75° and 60°, respectively. The design employs a basic module consisting of four cells, which are expanded along both the x-axis and y-axis by five units each (forming a 5 × 5 array), resulting in three types of metasurface arrays with single-degree-of-freedom characteristics. During the folding process, the deformation of the array is solely govened by the crease angle α, enabling continuous and coordinated motion of all units. This design demonstrates excellent mechanical performance, including high specific stiffness and large deformation capability.

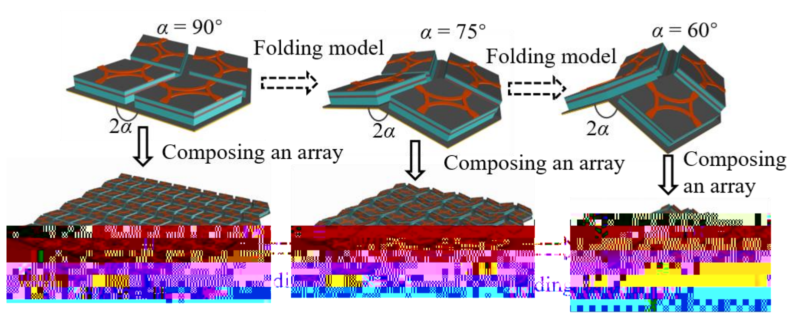

Fig. 2. Schematic diagram of the SDTAM Miura folded metasurface unit and metasurface array.

Full-wave electromagnetic simulation is employed to perform numerical analysis of the designed metasurface structure. Periodic boundary conditions are applied along the x- and y-directions to simulate the electromagnetic response of an infinite periodic array. The final optimized geometric parameters of the unit cell are as follows: $l = 40$ mm, $w = 2$ mm, $d = 3$ mm, $r = 19$ mm, β=20°, $h_1 = 1$ mm, $h_2 = 2$ mm.

Figure 3 shows the normalized reflection coefficient of the metasurface at different folding angles α. Specifically, Figs. 3(a) and 3(b) depict the reflection coefficients for linearly polarized (LP) and circularly polarized (CP) waves under normal incidence at α=90°, respectively, Figs. 3(c) and 3(d) correspond to α=75°, and Figs. 3(e) and 3(f) represent the situations of α=60°. In Figs. 3(a), 3(c) and 3(e), under LP wave incidence, the cross-polarized reflection coefficients r_{xy} and r_{yx} are nearly zero, while the co-polarized reflection coefficients r_{xx} and r_{yy} have magnitudes less than 0.2, indicating an extremely low reflectance response to LP waves. On the other hand, as illustrated in Figs. 3(b), 3(d) and 3(f), under CP wave incidence, although minor cross-polarized components r_{rl} and r_{lr} are generated, the co-polarized reflection coefficients r_{rr} and r_{ll} remain at low levels, demonstrating excellent low-reflectance characteristics for CP waves. The simulation results reveal that the proposed metasurface exhibits superior low-reflectance performance for both LP and CP electromagnetic waves across multiple configurations, including flat and various folded states, showcasing strong polarization insensitivity and structural robustness.

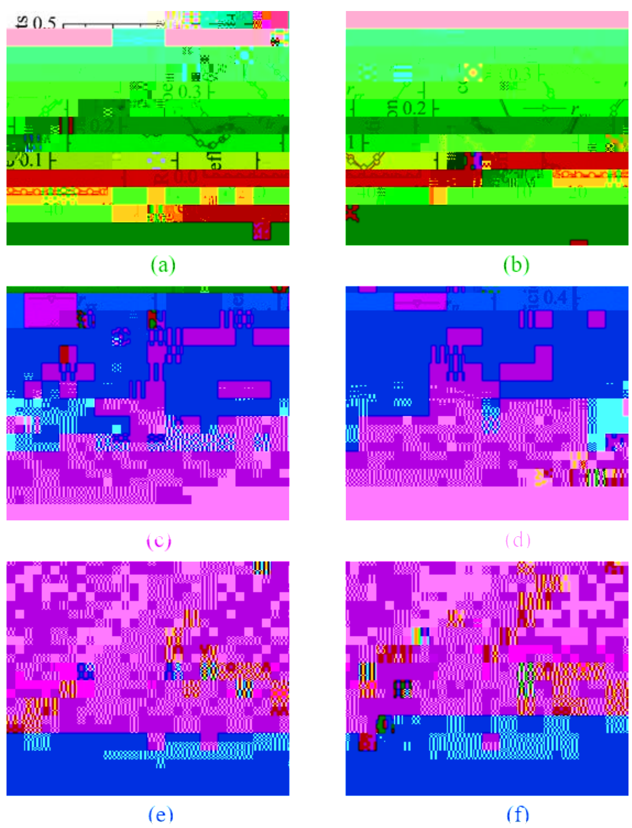

Fig. 3. Simulation results of normalized reflection coefficients for LP and CP incident waves under normal incidence: (a) α=90°, LP incident, (b) α=90°, CP incident, (c) α=75°, LP incident, (d) α=75°, CP incident, (e) α=60°, LP incident, and (f) α=60°, CP incident.

Optical Materials EXPRESS

The geometric dimensions of the metasurface unit cell shown in Fig. 1(c) under LCP wave incidence were determined by parameter sweeping. Figure 4 presents the reflection coefficient curves for arc radius $r = 15$ mm, 19 mm, and 24 mm, respectively. It can be observed that when $r = 19$ mm, the unit cell exhibits the lowest and flattest reflection response across the entire target frequency band, corresponding to the optimal impedance matching condition of the equivalent circuit. To elucidate the operating mechanism and the tunable absorption characteristics of a single metasurface unit cell, we present its equivalent circuit model (ECM) in Fig. 5(a). In this model, the top ITO patterned structure is equivalent to the first RLC series resonant network (R_1, C_1, L_1), while the middle ITO structure is equivalent to the second RLC series resonant network (R_2, C_2, L_2). The PET and PMMA dielectric layers are represented as transmission line segments with characteristic impedances: the first dielectric combination (PET + PMMA of thickness h1) is equivalent to transmission line TL1 (with electrical length corresponding to thickness t + h1), and the thicker dielectric combination composed of the middle PET layer, PMMA of thickness h1 and the bottom PET layer is equivalent to transmission line TL2 (with electrical length corresponding to thickness 2t + h2). Using Advanced Design System (ADS) software, we accurately extracted and optimized all lumped element parameters of each transmission line segment. Based on this ECM, the impedance matching condition at different frequencies can be conveniently analyzed, providing an intuitive explanation for the formation mechanism of absorption peaks and reflection dips: when the equivalent input impedance of the structure matches the free-space impedance, the incident electromagnetic wave energy is effectively absorbed; otherwise, it manifests as strong reflection. As shown in Fig. 5(b), the reflection coefficients calculated by ADS are compared with the full-wave simulation results obtained from CST Microwave Studio, and the two are in good agreement. This fully demonstrates that the ECM can accurately predict the absorption performance of the single metasurface unit cell. The optimized circuit parameters from ADS are: $R_1 = 840\ \Omega$, $L_1 = 0.7$ nH, $C_1 = 33.965$ pF, $R_2 = 262.5\ \Omega$, $L_2 = 14.575$ nH, $C_2 = 6.88$ pF, $Z_0 = 377\ \Omega$.

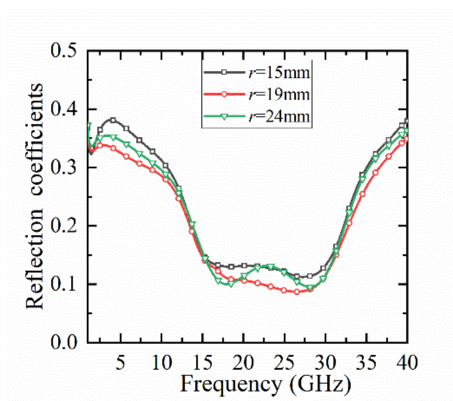

Fig. 4. Simulated reflection coefficients of the unit cell in the planar state ($\alpha = 90°$) under normal incidence for different arc radii r: 15 mm, 19 mm, and 24 mm.

Optical Materials EXPRESS

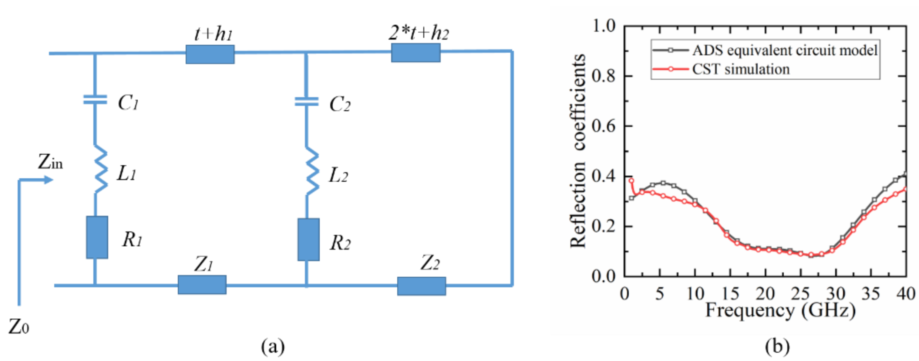

Fig. 5. Equivalent circuit model of the single metasurface unit cell in the planar state ($\alpha = 90°$): (a) schematic of the ECM, and (b) comparison of reflection coefficients obtained from ADS circuit simulation and CST full-wave simulation.

3. Simulation and analysis of RCS reduction characteristics

3.1. RCS reduction of planar and two-dimensional folded metasurfaces

The Miura-ori folding structure enables large-scale, coordinated deformation of rigid panels in three-dimensional space through a single-degree-of-freedom folding mechanism. In the folded state, adjacent unit cells are connected via creases, forming a non-planar periodic array. According to Floquet's theorem, the reflected field from such a periodic electromagnetic structure can be decomposed into a series of spatial harmonics. When the array period exceeds the operating wavelength, higher-order diffraction modes (m=±1,±2, . . .) are excited in addition to the main reflected beam ($m = 0$), scattering the incident electromagnetic energy into multiple directions. Consequently, the structure can not only dissipate electromagnetic energy through dielectric loss via embedded absorptive materials, but also synergistically reduce the RCS by leveraging structural scattering effects induced by its geometric configuration.

Compared to conventional planar absorbers, the reconfigurable absorbing metasurface based on the Miura-ori folding design introduces a prominent structural scattering mechanism. As shown in Fig. 1(b), each rhombic unit has a side length l and an acute angle of $90°-\beta$. A unit cell is composed of four such rhombi arranged in a tessellated configuration. Defining the folding angle as α, the effective period in the x-direction is given by:

$$d_x = 2l\sin(\alpha) \tag{1}$$

The angle of the grating flap can be calculated by the grating equation [31] :

$$\sin\theta_m = \frac{m\lambda}{d_x}, m = \pm 1, \pm 2, \ldots \tag{2}$$

Only physically realizable angles that satisfy condition $|\sin\theta| \leq 1$ are retained. The grating lobe angles for the three folding states, calculated using the aforementioned formulas, are summarized in Table 1. The results of the simulation are basically consistent with those of theoretical calculation. The difference between the calculated and simulated sidelobe angles mainly arises from the simplifying assumptions used in the analytical model. The grating-equation-based calculation assumes an ideal infinite periodic structure with simplified effective periods, whereas the full-wave simulation includes finite-array effects, inter-cell coupling, edge diffraction, and nonuniform phase/current distributions in the folded geometry.

Integrating absorptive metasurfaces as the skin of large-scale deformable structures is an effective strategy for achieving dynamic RCS reduction. In this study, the scattering characteristics

Table 1. Metasurface gate flap Angle parameters (Unit: °)

α	The θ angle of the side lobe of the plane φ=0°
90°	Calculation results: ±22.0°, ±48.6°
	Simulation results: ±23.7°, ±52.9°
75°	Calculation results: ±11.2°,±22.8°,±35.6°, ±50.9°
	Simulation results: ±11.07°, ±23.06°, ±35.55°, ±50.0°
60°	Calculation results: ±12.5°,±25.7°,±40.5°,±60.0°
	Simulation results: ±12.3°, ±25.8°, ±40.6°, ±60°

of the SDTAM are investigated under three typical configurations during large-scale morphing, under normal incidence of electromagnetic waves with different polarizations. Figure 6 presents the monostatic RCS reduction performance of the SDTAM over the frequency range of 1 GHz to 40 GHz, for both LP and CP normal incidence. It is observed that as the folding angle decreases, the 10 dB monostatic RCS reduction bandwidth progressively broadens. In the most compact folded configuration (α=60°), the SDTAM achieves over 10 dB RCS reduction for both LP and CP waves across a band from 4.1 to 40 GHz, corresponding to a relative bandwidth of 163%. These results demonstrate excellent wideband monostatic RCS reduction performance and strong polarization insensitivity under normal incidence of both LP and CP waves.

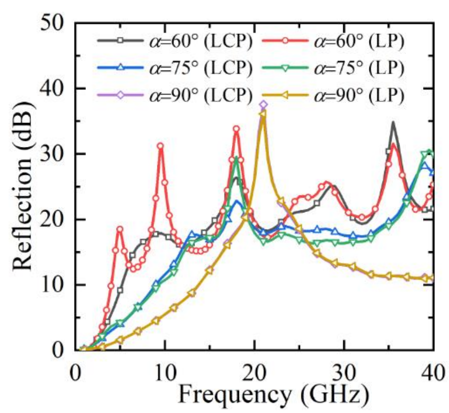

Fig. 6. Simulation results of monostatic RCS reduction under LP and CP plane waves vertically incident on SDTAM metasurface.

To further elucidate the physical mechanism underlying the enhanced absorption in the folded states, Fig. 7 presents the surface current distributions on the top patterned ITO layer at 20 GHz under normal incidence of left-handed circularly polarized (LCP) waves for the three folding angles. In the planar state ($\alpha = 90°$), strong currents are concentrated on the ITO patches, indicating that the absorption primarily originates from the intrinsic LC resonance of the patch structure. As the folding angle decreases to 75°, the currents on the patches are weaken, while those along the creases and inter-cell gap regions are enhanced, particularly the currents along the Miura-fold valleys become significantly stronger. At $\alpha = 60°$, the gap currents are further intensified (especially at the ridges), and the patch currents continue to decline. This evolution indicates that folding reduces the inter-unit spacing, strongly confining the electromagnetic energy within the gap regions, and shifts the peak surface currents from the patch surfaces to the folding creases and inter-cell gaps. Consequently, the primary dissipation site of the incident energy moves from the intrinsic resonant regions of the patches to the gap regions. The incident wave energy is locally enhanced in the narrow gaps and is efficiently absorbed through strong ohmic losses in the ITO resistive films at the gaps, rather than relying on resonant dissipation on the patch surfaces. Such a transition in dissipation mode optimizes the impedance matching and energy loss distribution, thereby providing an underlying explanation for the superior absorption performance of the compact folded state ($\alpha = 60°$) at lower frequencies.

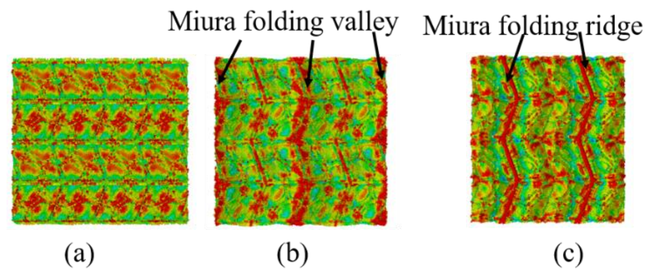

Fig. 7. Surface current distributions on the top patterned ITO layer at 20 GHz under LCP normal incidence for different folding angles: (a) $\alpha = 90°$, (b) $\alpha = 75°$, and (c) $\alpha = 60°$.

Figure 8 presents the bistatic RCS patterns of the SDTAM metasurface under normal incidence at 20 GHz, in comparison with a perfectly electric conducting (PEC) plate with identical dimensions. It can be observed that the PEC plate produces a strong, pencil-like main lobe in the specular reflection direction, resulting in significant backscattering. In contrast, the SDTAM metasurface effectively redistributes the incident energy into multiple diffracted beams propagating in different spatial directions, demonstrating a pronounced beam-scattering effect. Compared to the PEC plate, the SDTAM achieves a backscattering reduction of over 15 dB in the backward direction.

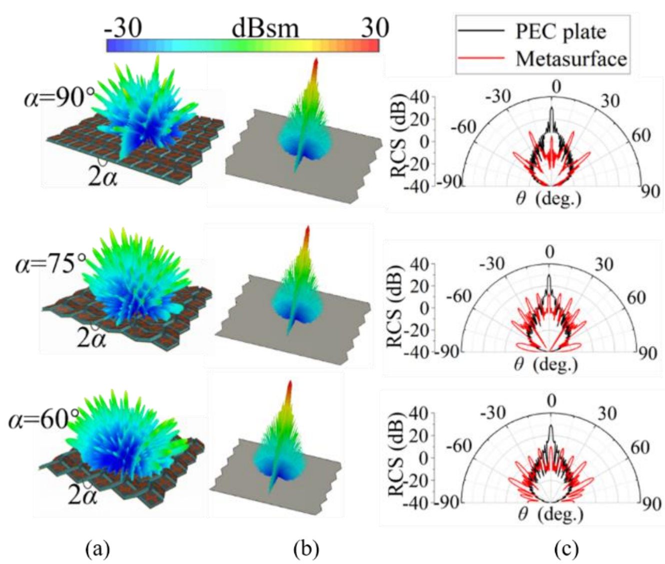

Fig. 8. Three-dimensional and two-dimensional far-field scattering simulation results of planar SDTAM, two folded SDTAM and PEC plane when x-polarized waves are normal incident at 20 GHz: (a) three-dimensional scattering results of SDTAM in the three states, (b) three-dimensional scattering results of PEC, and (c) two-dimensional E-plane scattering results of SDTAM and PEC surfaces.

Optical Materials EXPRESS

Further analysis reveals that as the folding angle α decreases, the effective periods dx and dy of the unit cell in the x and y directions are reduced. This leads to an increased number of diffraction orders that satisfy the grating equation, accompanied by shifts in the beam emission angles. Consequently, the proposed SDTAM metasurface achieves broadband RCS reduction through a dual-mechanism synergy: on one hand, the multilayer impedance-matching structure combined with resistive films enables efficient absorption of incident electromagnetic waves; on the other hand, the non-planar periodic geometry induces structural scattering, redirecting the residual reflected energy away from the backward direction.

In summary, the metasurface enables synergistic control of absorption and scattering throughout the folding process, significantly suppressing the backward RCS over a wide frequency band and under multiple polarization states. This work provides an effective solution for dynamic cloaking of deformable platforms.

With the advancement of multi-polarization radar detection technologies, the development of stealth techniques capable of countering electromagnetic threats under diverse polarization states has become critical. Therefore, a thorough investigation of metasurface responses to electromagnetic waves with varying polarization states is of great significance. Figure 9(a), Fig. 9(d) and Fig. 9(g) present contour maps of RCS reduction for three configurations, namely the flat state and two folded states, under normal incidence of TE-polarized waves with polarization angle φ varying from 0° to 90° in 10° increments. As φ increases, the RCS reduction performance of the flat state remains nearly unchanged. This stability is attributed to the structural periodic symmetry and the rotational symmetry of the top-layer unit pattern, demonstrating excellent polarization insensitivity of the planar configuration.

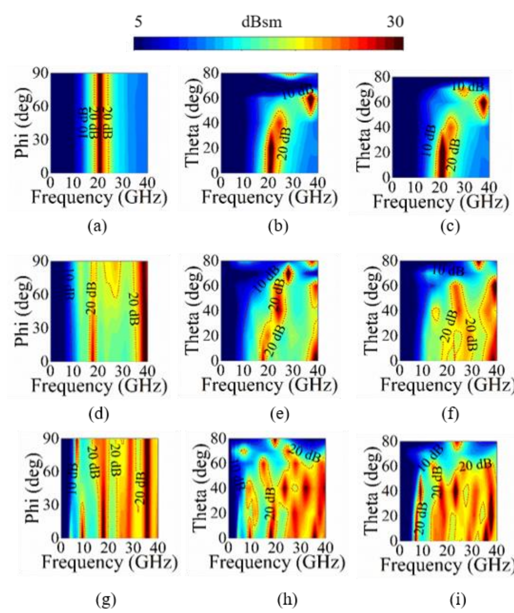

Fig. 9. Simulation results of RCS reduction contour maps of SDTAM with multipolarized waves and oblique incident electromagnetic waves: (a) monostatic RCS, α=90°, LP multipolarized normal incident, (b) bistatic RCS, α=90°, oblique incident of x waves, (c) bistatic RCS, α=90°, oblique incident of y waves, (d) monostatic RCS, α=75°, LP multipolarized normal incident, (e) bistatic RCS, α=75°, oblique incident of x waves, (f) bistatic RCS, α=75°, oblique incident of y waves, (g) monostatic RCS, α=60°, LP multipolarized normal incident, (h) bistatic RCS, α=60°, oblique incident of x waves, and (i) bistatic RCS, α=60°, oblique incident of y waves.

Optical Materials EXPRESS

In contrast, as the folding angle decreases, the RCS reduction bandwidth significantly broadens, and the frequency regions exhibiting deep RCS reduction become more extensive as illustrated in Figs. 9(d) and Fig. 9(g). This behavior arises from the reduced effective period of the unit cell after folding, which increases the number of diffraction orders satisfying the grating equation, thereby making more scattering energy into multiple spatial directions. Consequently, the proposed SDTAM exhibits outstanding RCS reduction performance across a wide range of polarization angles, confirming its robustness and effectiveness under multi-polarization illumination.

The aforementioned analysis primarily focuses on the scattering characteristics under normal incidence. However, in practical radar detection scenarios, electromagnetic waves often impinge on targets at oblique angles. Therefore, investigating the scattering response of the SDTAM to obliquely incident waves is of critical importance. Figures 9(b), 9(e), and 9(h) present contour maps of RCS reduction for x-polarized waves incident at various angles θ. As the incidence angle increases, the bistatic RCS reduction performance gradually degrades; nevertheless, broadband bistatic RCS reduction exceeding 10 dB is still achieved even at an extreme incidence angle of 70°. Similarly, Figs. 9(c), 9(f), and 9(i) show the results for y-polarized waves, demonstrating that the structure maintains strong RCS reduction capability at 70° incidence. These results indicate that the SDTAM metasurface exhibits robust scattering control for both x and y-polarized waves over a wide angular range.

In summary, the proposed SDTAM metasurface not only delivers excellent RCS reduction performance under multi-polarization conditions but also maintains effective stealth characteristics across a broad range of incidence angles. This highlights its potential for achieving dynamic, broadband, and wide-angle radar cross-section reduction in complex electromagnetic environments.

The distinction between the proposed SDTAM metasurface and conventional absorptive metasurfaces lies in the integration of a broadband absorbing structure with a Miura-ori-based reconfigurable architecture. The unique geometric configuration of the Miura-ori folding structure not only enables large-scale deformability but also induces structural scattering effects through its non-planar periodic arrangement. This mechanism divides the incident electromagnetic energy into three components: energy absorbed by the material, energy specularly reflected in the mirror direction, and energy scattered into non-backward directions. This enables the SDTAM to achieve synergistic RCS reduction through a combined “absorption + scattering” mechanism, effectively dissipating and redirecting incident electromagnetic energy.

Figure 10 illustrates the energy distribution characteristics of the three configurations, under normal incidence of LP waves. The calculation procedure is as follows: first, the discrete two-dimensional far-field radiation pattern data $P_{\mathrm{dB}}(\theta,\phi)$ are extracted from CST Microwave Studio, representing the power density in each direction (θ,ϕ) in the spherical coordinate system, with units in dB. Subsequently, these dB values are converted into linear power values using the following transformation formula [32]:

$$\boldsymbol{P}_{linear}(\theta, \varphi) = 10^{\frac{P_{db}(\theta,\varphi)}{10}} \tag{3}$$

In the spherical coordinate system, the total radiated energy can be calculated by surface integration [33,34]:

$$\boldsymbol{E} = \int_0^{\pi}\int_0^{2\pi} \boldsymbol{P}_{linear}(\theta, \varphi) \sin\theta d\theta d\varphi \tag{4}$$

The energy within a specified spatial region can be calculated using numerical integration methods [35]. Specifically, Einc is defined as the reflected energy from an ideal conductor (PEC) plate with the same size under normal incidence conditions. The specular reflection energy E_{refl} is determined by integrating over the angular ranges of $\theta\in[0°,...,5°]$ and $\phi\in[0°,...,360°]$.

Optical Materials EXPRESS

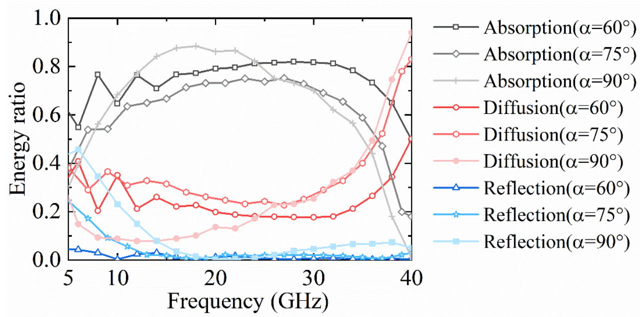

Fig. 10. Simulation results of the energy proportion of flat state and the two folded states as functions of frequency under LP wave normal incidence.

The structural scattering energy E_{scat} is obtained by integrating over the angular ranges of $\theta \in [5°,\ldots,180°]$ and $\phi \in [0°,\ldots,360°]$ for all non-specular directions. The absorbed energy E_{abs} is computed based on energy conservation:

$$E_{abs} = E_{inc} - E_{refl} - E_{scat} \tag{5}$$

Given that the underlying layer consists of a 6 Ω/sq ITO resistive film serving as a ground plane, transmission energy is negligible. Additionally, diffraction energy, already accounted for in the far-field scattering component, does not require separate consideration.

Figure 10 presents the variation of energy proportions with frequency for the flat state and two folded states under TE wave incidence. As the frequency increases, the proportion of absorbed energy initially rises, reaching a peak around 20 GHz before gradually declining. In contrast, the proportion of scattered energy decreases initially, hitting a minimum near 20 GHz before increasing again. At higher frequencies, the energy distribution is primarily governed by structural scattering. The proportion of specular reflection energy consistently decreases with increasing frequency. These results indicate that at lower frequencies, absorption mechanisms dominate RCS reduction, whereas at medium to high frequencies, structural scattering mechanisms become increasingly significant, working synergistically with absorption to achieve efficient stealth across the entire frequency range.

3.2. RCS reduction of curved conformal metasurfaces

Large-scale deformable structures often involve complex curved surfaces, making it essential to investigate the scattering characteristics of conformal metasurfaces on such highly deformed geometries. The bending deformation of the SDTAM metasurface array is primarily enabled by the unique negative Poisson's ratio property of the Miura-ori structure: when compressed in one direction, the structure expands perpendicularly. When a planar Miura-ori structure is rolled into a cylindrical shape, axial compression induces circumferential expansion, allowing it to perfectly conform to the geometric constraints of the cylinder. In addition, the zigzag folding pattern characterized by alternating creases in valleys generates periodically changing local curvatures during the deformation process. This curvature distribution is compatible with the constant Gaussian curvature of a cylindrical surface [36]. In summary, the cylindrical consistency of the Miura-ori structure is derived from its single DOF kinematics, the negative Poisson's ratio effect, and the curvature compatibility of the crease network.

Figure 11 presents a comparison of RCS scattering between the SDTAM metasurface and a bare cylindrical surface with identical size, under normal incidence of an x-polarized wave at 20 GHz and 30 GHz. The cylinder has a radius $r = 200$ mm with its axis aligned along the x-direction. The first column shows the 3D scattering radiation pattern of the metasurface, the second column depicts that of the bare cylindrical surface with the same curvature, and the third column illustrates the E-plane RCS comparison between the metasurface and bare surface. The results show that the scattering from the SDTAM metasurface is not confined to the plane perpendicular to the cylinder axis but spreads along the axial direction. This indicates significant suppression of the deterministic scattering field. Consequently, the Miura-ori-based metasurface demonstrates excellent conformability to curved surfaces and effective RCS reduction even under large-curvature cylindrical deformation.

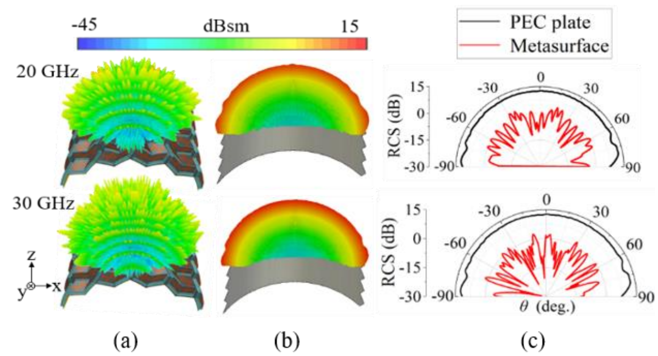

Fig. 11. Three-dimensional and two-dimensional far-field scattering simulation results of the cylindrical SDTAM and PEC along the y direction and the normal direction of the x-polarized wave: (a) three-dimensional scattering results of SDTAM, (b) three-dimensional scattering results of PEC surface, and (c) two-dimensional E-plane scattering results of SDTAM and PEC surfaces.

Figure 12 presents a similar comparison for a y-polarized wave incident normally on cylindrical metasurface and bare surface ($r = 200$ mm), with the cylinder axis aligned along the y-direction. Again, the first and second columns display the 3D scattering patterns of the SDTAM metasurface and the bare cylinder, respectively, while the third column provides the E-plane RCS comparison. It is observed that the scattering pattern of the SDTAM extends beyond the cross-sectional plane and spreads along the axial direction, further confirming the effective suppression of the SDTAM scattering field.

Figure 13 shows the monostatic RCS reduction performance of the conformal metasurface under different polarization states and cylinder axis orientations. Specifically, Fig. 13(a) corresponds to x-polarized incidence with the cylinder axis along x, Fig. 13(b) corresponds to y-polarized incidence with the axis still along x, Fig. 13(c) corresponds to x-polarized incidence with the axis along y, and Fig. 13(d) corresponds to y-polarized incidence with the axis along y. The monostatic RCS is analyzed as a function of frequency for metasurfaces conformed to cylinders of radii 200 mm, 300 mm, and 400 mm. Significant RCS reduction is achieved for all configurations. This reduction is attributed to the presence of multiple discontinuities at the Miura-ori folding joints, where multiple reflections and refractions occur within the gaps. These structural discontinuities generate strong scattered waves at certain frequencies, leading to interference among scattered fields and resulting in pronounced fluctuations in the RCS spectrum. Despite these ripples, all three conformal configurations achieve a monostatic RCS reduction exceeding 8 dB over the frequency band from 15 GHz to 40 GHz, demonstrating the broadband effectiveness and geometric adaptability of the proposed SDTAM design.

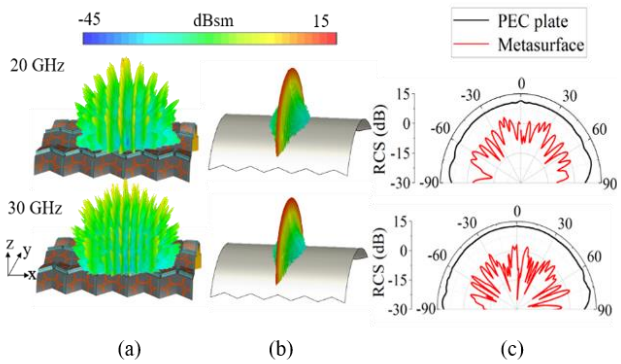

Fig. 12. Three-dimensional and two-dimensional far-field scattering simulation results of the cylindrical SDTAM and PEC along the *x* direction and the normal direction of the y-polarized wave: (a) three-dimensional scattering results of SDTAM, (b) three-dimensional scattering results of PEC surface, and (c) two-dimensional E-plane scattering results of SDTAM and PEC surfaces.

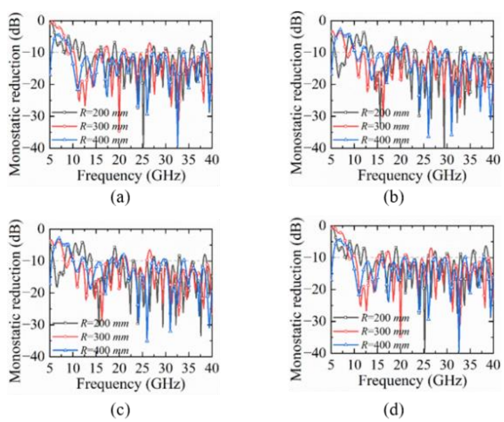

Fig. 13. Monostatic RCS simulation results of curved SDTAM with (a) *x*-direction and *x*-polarized waves normal incident, (b) *x*-direction and *y*-polarized waves normal incident, (c) *y*-direction and x-polarized waves normal incident, and (d) *y*-direction and *y*-polarized waves normal incident.

4. Experiment and verification

To validate the effectiveness of the proposed metasurface in RCS backscattering suppression, a 376 mm × 400 mm SDTAM metasurface sample was fabricated, as shown in Fig. 14(a). The fabrication process is detailed as follows: Initially, a 23 nm thick ITO film was deposited onto a 0.188 mm thick PET dielectric substrate using magnetron sputtering to serve as the top layer. Subsequently, continuous ITO resistive films were patterned in the intermediate layer. Next, the layers were sequentially bonded together with adhesive: top PET-resistive film-PMMA -intermediate PET-resistive film-PMMA. Finally, the bottom PET layer was processed, and grooves for facilitating folding were etched into the bottom PET structure via photolithography. After completing these steps, the discrete structures were affixed to the bottom PET framework. The test environment is shown in Fig. 14(b). Figure 14(c) shows the dedicated support structure fabricated using 3D printing technology. Figure 14(d) shows the overall installation state after attaching the metasurface sample to the support structure, it can be seen that the metasurface is firmly fixed and the structure is stable.

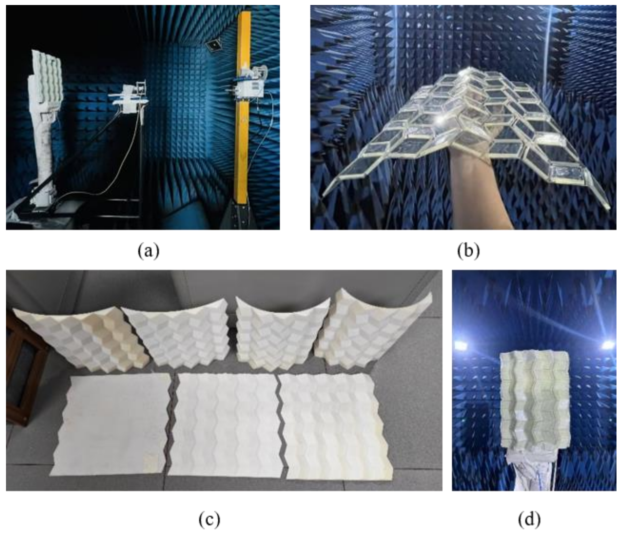

Fig. 14. Test scenarios and SDTAM processing samples: (a) test scenario, and (b) SDTAM processing samples, and (c) the specialized support structure manufactured by 3D printing technology, and (d) SDTAM close-up view

Before the measurement, the horn antennas and the measurement chain were calibrated to reduce system errors. During the measurements, an Agilent E8363C PNA network analyzer connected to two standard gain horn antennas was used for transmitting and receiving signals. To mitigate environmental background noise, a CMP-18G40G-3327-K signal amplifier was employed to boost the transmission power, enhancing the signal-to-noise ratio. In the bistatic scattering measurement, the transmitted signal from the vector network analyzer was amplified and fed into the transmitting horn antenna, and the scattered field from the metasurface sample was collected by the receiving horn antenna at various observation angles. The measured scattering patterns were then normalized to the maximum received response within the scanning angular range.

Figure 15 presents the monostatic RCS reduction performance of the planar-state SDTAM. Under x-polarized wave normal incidence, the structure achieves an RCS reduction exceeding 10 dB over the frequency range of 13.8 GHz to 40 GHz. Similarly, under y-polarized normal incidence, a greater than 10 dB RCS reduction is realized across the same band. The close agreement between simulated and measured results validate the structure's excellent broadband and dual-polarization electromagnetic wave absorption capability.

Figure 16 shows the normalized relative two-dimensional bistatic E-plane scattering patterns of the planar-state SDTAM under incidence of both x- and y-polarized waves. For x-polarized wave excitation, scattering peaks appear at 0°, ±22°, and ±48.5°. Under y-polarized incidence, the peak directions are almost identical, occurring at 0°, ±22°, and ±48.5°. These lobes correspond to the main lobe and grating lobes of the periodic structure, consistent with predictions from the grating equation. The measured results confirm that the planar-state SDTAM exhibits outstanding scattering suppression over a broad frequency band, demonstrating its high-efficiency electromagnetic absorption characteristics.

Figure 17 illustrates the monostatic RCS reduction of the folded-state SDTAM at a folding angle of α=60°. Under x-polarized normal incidence, the structure achieves over 10 dB RCS reduction

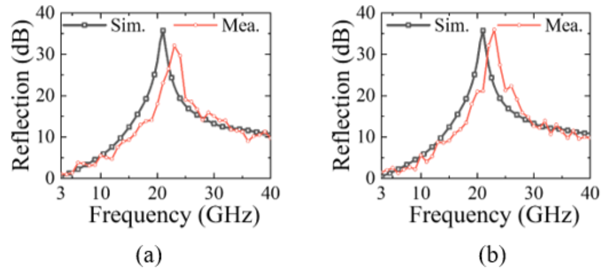

Fig. 15. Simulation and measured results of monostatic RCS reduction of planar state SDTAM of α=90° when LP wave normal incident: (a) x-polarized wave incident, and (b) y-polarized wave incident.

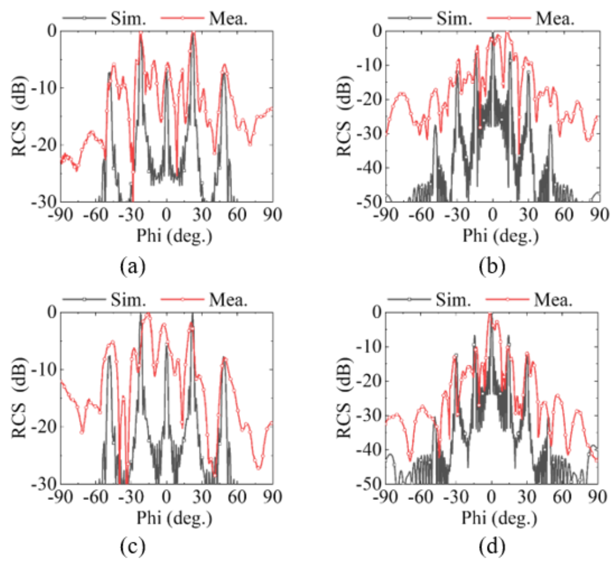

Fig. 16. Simulated and measured normalized relative bistatic two-dimensional E-plane scattering patterns of the planar-state SDTAM (α = 90°) under normal incidence of LP waves. (a) x-polarized waves are incident at 20 GHz, (b) x-polarized waves are incident at 30 GHz, (c) y-polarized waves are incident at 20 GHz, and (d) y-polarized waves are incident at 30 GHz.

from 4.1 GHz to 40 GHz, corresponding to a bandwidth of 163%. Under y-polarized normal incidence, similarly broadband RCS reduction is observed. The strong consistency between simulation and measurement further verifies the robustness of the design. Figure 18 shows the normalized relative two-dimensional bistatic E-plane scattering patterns of the folded-state SDTAM (α= 60°) under incidence of both x- and y- polarized waves. For x- polarized normal incidence, scattering peaks occur at 0°, ±12.6°, ±25.2°, ±40.5°, and ±60.2°. Under y-polarized normal incidence, the peak locations almost remain unchanged, indicating that the structure maintains good polarization symmetry even after folding. This multi-lobe radiation pattern arises from the reduced effective periodicity of the unit cells upon folding, which excites higher-order diffraction modes and enables spatial dispersion of scattered energy. The experimental results demonstrate that the folded-state SDTAM of α=60° not only retains strong absorption performance but also enhances RCS reduction through structural scattering, effectively combining dissipation and diffusion mechanisms for superior electromagnetic stealth.

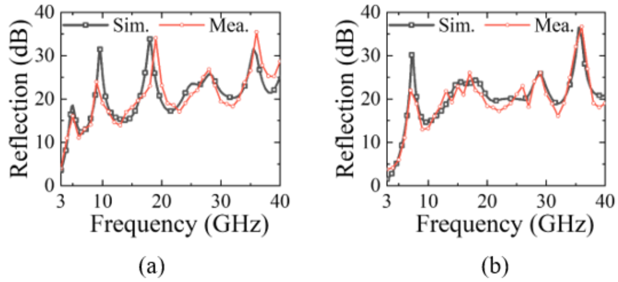

Fig. 17. Simulation and measured results of monostatic RCS reduction in bending state SDTAM of α=60° when LP wave incident, (a) *x*-polarized wave incident, and (b) *y*-polarized wave incident.

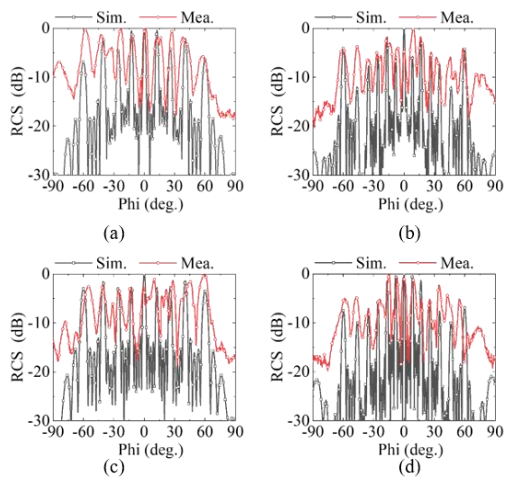

Fig. 18. Simulated and measured normalized relative bistatic two-dimensional E-plane scattering patterns of the SDTAM in the folded state (α=60°) under normal incidence of LP waves. (a) *x*-polarized waves are incident at 20 GHz, (b) *x*-polarized waves are incident at 30 GHz, (c) *y*-polarized waves are incident at 20 GHz, and (d) *y*-polarized waves are incident at 30 GHz.

The discrepancies between simulation and measurement can be primarily attributed to the following factors: misalignment of the transmitting and receiving horn antennas; dimensional tolerances and layer-to-layer misregistration during sample fabrication; and variations in dielectric properties caused by non-uniform adhesive thickness. These practical imperfections inevitably introduce phase and amplitude deviations in the measured electromagnetic response. The experimental results systematically validate that the SDTAM metasurface exhibits excellent absorption-scattering synergistic RCS reduction performance in both the planar and folded states. The structure demonstrates robust electromagnetic stealth capabilities over a broad frequency band, under dual-polarization incidence, and across large folding angles. These findings provide critical experimental evidence and valuable engineering guidance for the development of dynamically reconfigurable radar-invisible skins applicable to deformable platforms.

Optical Materials EXPRESS

5. Conclusion

In this paper, a stretchable, deformable and optically transparent metasurface for multipolar RCS reduction is proposed. The SDTAM is constructed by integrating indium ITO resistive films with a transparent Miura-origami dielectric structure. Simulation results demonstrate that during the folding process, the SDTAM can achieve a common bandwidth of 13.8 GHz to 40 GHz for monostatic RCS reduction exceeding 10 dB for both LP and CP waves, exhibiting excellent broadband absorption performance. Notably, the bistatic RCS reduction remains stable even under large-angle oblique incidence for both polarizations, indicating strong angular independence and robustness. Furthermore, the SDTAM exhibits outstanding conformal capability, enabling it to be tightly wrapped around cylindrical surfaces. When conformed to cylinders with radii ranging from 200 to 400 mm, the metasurface maintains a broadband RCS reduction of over 8 dB across the operational band, validating its effectiveness on curved platforms.

Funding. National Natural Science Foundation of China (U2241204, U2541209).

Disclosures. The authors declare no conflict of interest.

Data availability. Data underlying the results presented in this paper are not publicly available at this time but maybe obtained from the authors upon reasonable request.

References

1. Q. He, S. Sun, S. Xiao, *et al.*, "High efficiency metasurfaces: principles, realizations, and applications," Adv. Opt. Mater. **6**(19), 1800415 (2018).
2. X. Gong and X. Wan, "Automatic target recognition based on RCS and angular diversity for multistatic passive radar," IEEE Trans. Aerosp. Electron. Syst. **58**(5), 4226–4240 (2022).
3. Jr. J. W. Crispin, ed., *Methods of Radar Cross-Section Analysis*, (Elsevier, 2013).
4. J. Palmer, D. Cristallini, and H. Kuschel, "Opportunities and current drivers for passive radar research," *IEEE Radar Conf.* (2015).
5. A. Muniyasamy and K. Rajakani, "UWB radar cross section reduction in a compact antipodal Vivaldi antenna," AEU Int. J. Electron. Commun. **99**, 369–375 (2019).
6. N. I. Landy, S. Sajuyigbe, J. J. Mock, *et al.*, "Perfect metamaterial absorber," Phys. Rev. Lett. **100**(20), 207402 (2008).
7. P. Marin, D. Cortina, and A. Hernando, "Electromagnetic wave absorbing material based on magnetic microwires," IEEE Trans. Magn. **44**(11), 3934–3937 (2008).
8. F. Costa, A. Monorchio, and G. Manara, "Analysis and design of ultra thin electromagnetic absorbers comprising resistively loaded high impedance surfaces," IEEE Trans. Antennas Propag. **58**(5), 1551–1558 (2010).
9. Z. Du, J. Liang, T. Cai, *et al.*, "Ultra-light planar meta-absorber with wideband and full-polarization properties," Opt. Express **29**(5), 6434–6444 (2021).
10. C. Lee, K. Kim, P. Park, *et al.*, "Ultra-wideband electromagnetic composite absorber based on pixelated metasurface with optimization algorithm," Materials **16**(17), 5916 (2023).
11. Z. Song, J. Zhu, L. Yang, *et al.*, "Wideband metasurface absorber (metabsorber) using characteristic mode analysis," Opt. Express **29**(22), 35387–35399 (2021).
12. Z. Qin, K. Zhou, Y. Li, *et al.*, "Dynamic meta-holography from linear to nonlinear enabled by transmissive independently addressable metasurface," Laser Photonics Rev. (2026) (in press).
13. L. Jiang, Y. Li, H. Yang, *et al.*, "Beam scanning with ultra-low sidelobes and in-band ultra-low scattering characteristics empowered by single space-time-coding radiation-scattering metasurface," Adv. Sci. **12**(11), 2413429 (2025).
14. Z. Qin, K. Zhou, Y. Li, *et al.*, "Dynamically continuous tunable metasurface with switchable transmission and absorption modes," IEEE Trans. Microw. Theory Techn. **74**(6), 4908–4920 (2026).
15. Z. Li, J. Wang, and W. Zheng, "Deformable transparent metasurface with multipolarization absorptive characteristics for RCS reduction," IEEE Antennas Wirel. Propag. Lett. **73**(3), 1768–1776 (2025).
16. P. Min, Z. Song, L. Yang, *et al.*, "Multispectral meta-film design: simultaneous realization of wideband microwave absorption, low infrared emissivity, and visible transparency," Opt. Express **30**(18), 32317–32332 (2022).
17. X. Hu, Y. Wang, Z. Wan, *et al.*, "Design and analysis of an optically transparent ultra-wideband absorber covering C-, X-, Ku-, K-, Ka-bands," Opt. Mater. Express **12**(4), 1512–1521 (2022).
18. H. Dai, S. Li, P. Dong, *et al.*, "Design of an ultra-wideband transparent wave absorber," Materials **16**(17), 5962 (2023).
19. Z. Ren, H. Yin, X. Sun, *et al.*, "An angularly stable and optically transparent broadband conformal microwave absorber using a diamond-shaped pattern," Opt. Mater. **131**, 112689 (2022).
20. Z. Song, P. Min, L. Yang, *et al.*, "A bilateral coding metabsorber using characteristic mode analysis," IEEE Antennas Wirel. Propag. Lett. **21**(6), 1228–1232 (2022).
21. Z. Zhu, Y. Li, Z. Qin, *et al.*, "Miura origami based reconfigurable polarization converter for multifunctional control of electromagnetic waves," Photonics Res. **12**(3), 581–586 (2024).

Optical Materials EXPRESS

22. Z. Song, J.-F. Zhu, X. Wang, *et al.*, "Origami metamaterials for ultra wideband and large depth reflection modulation," Nat. Commun. **15**(1), 3181 (2024).
23. X. Jiang, L. Zhang, B. Zou, *et al.*, "Metasurface design and scattering characteristics analysis of Miura Ori folded structure," *Proc. UCMMT*, pp. 1–4 (2022).
24. F. Meng, S. Chen, W. Zhang, *et al.*, "Negative Poisson's ratio in graphene Miura origami," Mech. Mater. **155**, 103774 (2021).
25. M. Li, L. Jing, S. Xu, *et al.*, "Origami Metawall: Mechanically controlled absorption and deflection of light," Adv. Sci. **6**(23), 1901434 (2019).
26. T.-L. Pham, K. B. Xuan, B. S. Tung, *et al.*, "Origami-based stretchable bi-functional meta materials: reflector and broadband absorber," Appl. Phys. **54**, 165111 (2021).
27. Z. Zhu, H. Wang, A. Li, *et al.*, "Origami-based metamaterials for dynamic control of wide-angle absorption in a reconfigurable manner," IEEE Trans. Antennas Propag. **70**(6), 4558–4568 (2022).
28. H. Huang, H. Xia, Z. Guo, *et al.*, "A polarization-independent and broadband microwave metamaterial absorber based on three-dimensional structure," J. Mod. Opt. **65**(13), 1521–1528 (2018).
29. S. A. Nauroze, L. S. Novelino, M. M. Tentzeris, *et al.*, "Continuous-range tunable multilayer frequency-selective surfaces using origami and inkjet printing," Proc. Natl. Acad. Sci. **115**(52), 13210–13215 (2018).
30. X. Chen, W. Li, Z. Wu, *et al.*, "Origami-based microwave absorber with a reconfigurable bandwidth," Opt. Lett. **46**(6), 1349 (2021).
31. J. von Fraunhofer, "On the diffraction of light," Ann. Phys. **74**, 337–378 (1821).
32. J. D. Kraus and R. J. Marhefka, *Antennas: For All Applications*, 3rd ed. (McGraw-Hill, 2002), ch. 2.
33. C. A. Balanis, *Antenna Theory: Analysis and Design*, 4th ed. (Wiley, 2016), ch. 2, 3.
34. M. I. Skolnik, *Introduction to Radar Systems*, 3rd ed. (McGraw-Hill, 2001), ch. 8.
35. W. H. Press, S. A. Teukolsky, W. T. Vetterling, *et al.*, *Numerical Recipes: The Art of Scientific Computing*, 3rd ed. (Cambridge Univ. Press, 2007), ch. 4.
36. F. Wang, H. Gong, X. Chen, *et al.*, "Folding to curved surfaces: A generalized design method and mechanics of origami-based cylindrical structures," Sci. Rep. **6**(1), 33312 (2016).